

# Frequency-Scaled Curvature as a Proxy for Topographic Site-Effect Amplification and Ground-Motion Variability

by Emeline Maufroy, Víctor M. Cruz-Atienza, Fabrice Cotton,\* and Stéphane Gaffet†

**Abstract** We introduce a new methodology to predict the topographic site-effect amplification. Ground motions obtained from a large database of 3D earthquake simulations show that the curvature of the Earth's surface, defined as the second spatial derivative of the elevation map, is correlated with the topographic site amplification. The highest correlation between the frequency-dependent topographic amplification and the topographic curvature is reached when the curvature is smoothed over a characteristic length equal to the  $S$  wavelength divided by two (i.e., frequency-scaled curvature [FSC]). This implies the amplification is caused by topographic features for which horizontal dimensions are similar to half of the  $S$  wavelength. The largest ground-motion variabilities are found at sites located on slopes and on the largest summits, whereas intermediate variabilities occur over narrow ridges and a stable behavior in the bottom valleys. The FSC proxy allows the identification of topographic features with similar characteristic dimensions and probabilistic estimates of amplification values accounting on the variability of ground motions due to source–site interactions. Amplification estimates using the FSC proxy are robust and easily computed from digital elevation maps provided that reasonable values of  $S$ -wave velocities are available in the area of interest.

## Introduction

The topographic site effect is a complex frequency-dependent 3D phenomenon (Sánchez-Sesma, 1983; Geli *et al.*, 1988; Sánchez-Sesma and Campillo, 1991; Bouchon and Barker, 1996; Buech *et al.*, 2010; Maufroy *et al.*, 2012; Massa *et al.*, 2014) that produces large ground-motion amplifications in the vicinity of summits (Gaffet *et al.*, 2000; Buech *et al.*, 2010; Massa *et al.*, 2010) and may cause damages during large earthquakes (Çelebi, 1987; Kawase and Aki, 1990; Bouchon and Barker, 1996; Spudich *et al.*, 1996; Assimaki, Gazetas, and Kausel, 2005; Hough *et al.*, 2010; Pischituta *et al.*, 2010). The seismic waves propagating in areas with topographies are generally disrupted at frequencies above 1 Hz (Boore, 1973; Sánchez-Sesma and Campillo, 1991; Durand *et al.*, 1999; Assimaki, Kausel, and Gazetas, 2005; Pischituta *et al.*, 2010).

Numerous studies on topographic site effects have provided interesting findings to forecast the amplification produced by the topography (Geli *et al.*, 1988; Assimaki, Kausel, and Gazetas, 2005; Bouckovalas and Papadimitriou,

2005). Most of them propose models based on simple 2D geometrical considerations (e.g., surface slopes, height, and/or width of hills) to estimate the amplification due to isolated peaks (e.g., Sánchez-Sesma, 1983; Geli *et al.*, 1988; Ashford *et al.*, 1997; Bouckovalas and Papadimitriou, 2005). However, the complexity of the phenomenon (i.e., frequency and source dependencies, intrinsic 3D effects) makes it difficult to provide general models able to predict motion patterns in realistic topographic configurations. Recently, 3D numerical simulations of ground motions have been useful to estimate site effects on realistic, intricate topographies (Lee, Chan, Komatitsch, *et al.*, 2009; Lee, Komatitsch, Huang, *et al.*, 2009; Chaljub *et al.*, 2010; Maufroy *et al.*, 2012; De Martin *et al.*, 2013). Nonetheless, this kind of sophisticated simulations remains computationally expensive (Chaljub *et al.*, 2010) and thus unsuitable for common seismic-hazard studies. A simple and robust method, based on geometrical properties of the Earth's surface, integrating most of the 3D effects and source variability, would be extremely useful for practical purposes.

In this work, we introduce a new methodology to predict topographic site effects based on the Earth's surface curvature, which is a single metric easily derived from digital elevation maps (DEMs). Our results were obtained from a large set of 3D numerical simulations designed to isolate

\*Also at German Research Centre for Geosciences (GFZ), Helmholtzstrasse 6, 14467 Potsdam, Germany.

†Also at LSBB, UMS 3538, Université de Nice Sophia-Antipolis, Université d'Avignon et des Pays de Vaucluse, CNRS, Aix Marseille Université, Observatoire de la Côte d'Azur, La grande combe, F-84400 Rustrel, France.

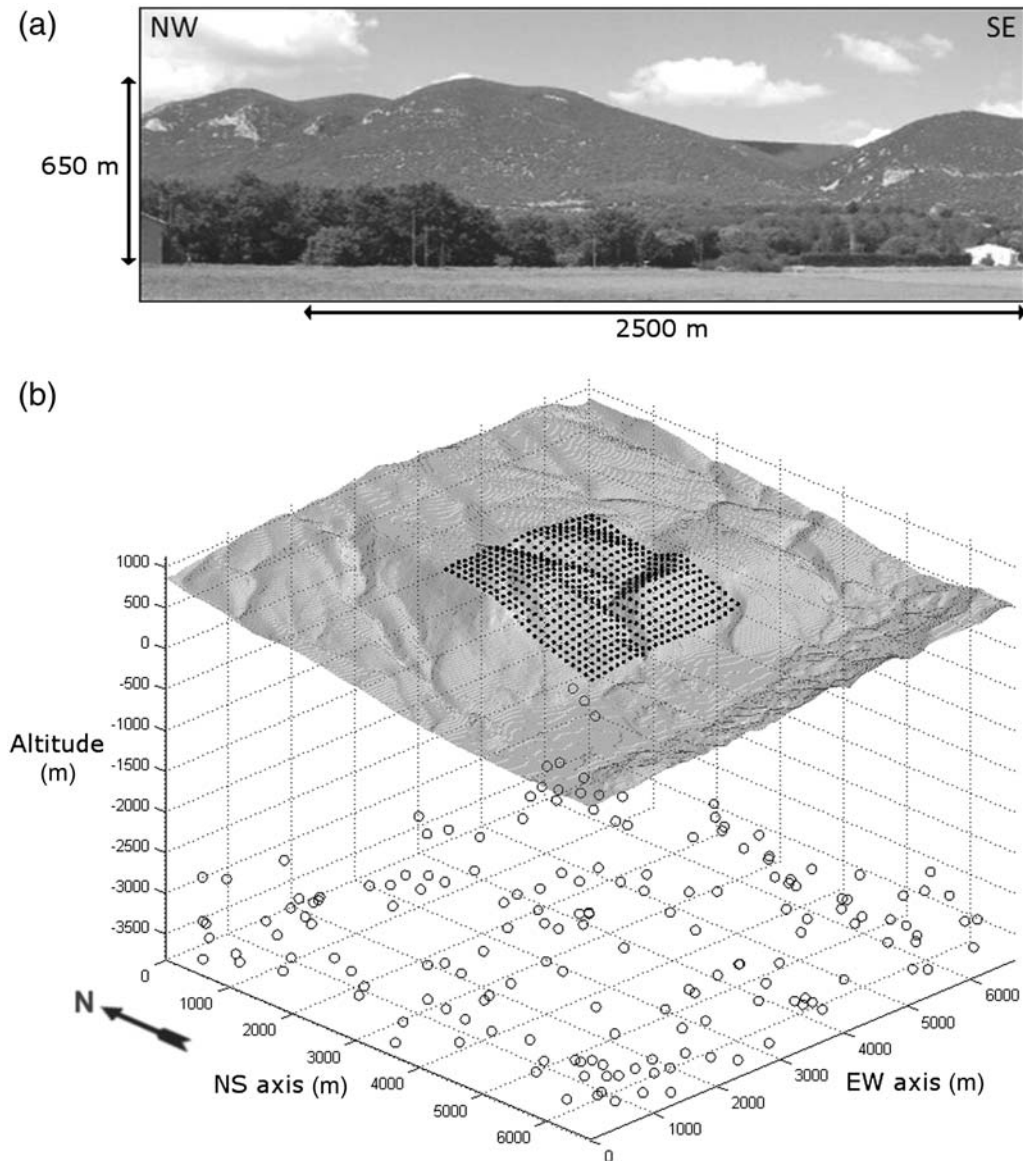


**Figure 1.** (a) Photograph of the topography surrounding the inter-Disciplinary Underground Science and Technology laboratory (i-DUST/LSBB) area, which is part of the wider Albion plateau (France), (b) 3D location of the 200 random double-couple point sources (empty circles) and the square array of 576 virtual receivers (black dots, one station every 100 m) relative to the surface topography shown in transparency. Spatial unit is in meters.

the topographic effects from others due to different geological features (e.g., low-velocity layers).

We also evaluate the impact of surface topography on the ground-motion variability. Such analysis is motivated by the fact that the random variability associated to ground-motion predictions ( $\sigma$ ) strongly influences the seismic-hazard curve computation, in particular for long return periods (Bommer and Abrahamson, 2006). The understanding of the physical causes of ground-motion variability has not been explored yet, and topography is one of the suggested explanations (e.g., Rai *et al.*, 2012; Rodriguez-Marek *et al.*, 2013). Our simulations provide a unique opportunity to analyze the spatial variations of the ground-motion variability and discuss topography proxies that may help to identify sites where

ground motions are more variable and highly dependent on source–site configurations.

### Ground-Motion Synthetic Database

In the previous work (Maufroy, 2010; Maufroy *et al.*, 2012), we performed 200 ground-motion simulations generated by double-couple point sources in the mountainous area surrounding the inter-Disciplinary Underground Science and Technology laboratory (i-DUST/LSBB), Rustrel, France (Fig. 1). To achieve numerical accuracy up to 4 Hz including the irregular topography shown in Figure 1b, we used the partly staggered finite-difference code SHAKE3D (Cruz-Atienza, 2006; Cruz-Atienza, Virieux, and Aochi, 2007; Cruz-Atienza, Virieux,

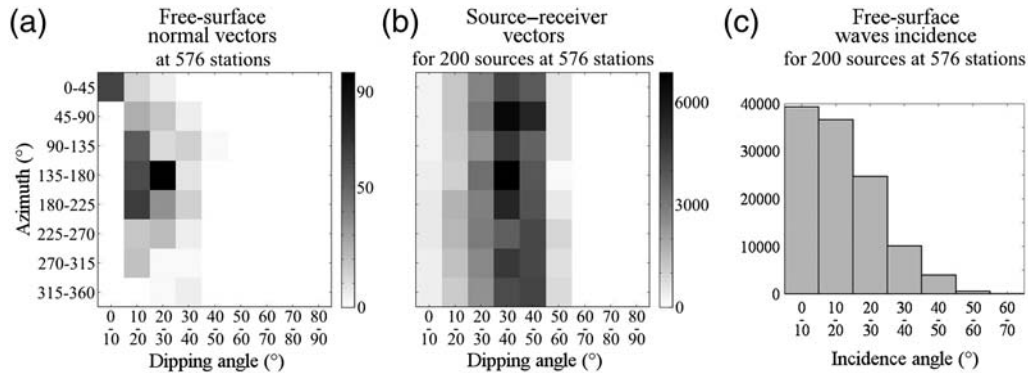


**Figure 2.** Characteristics of vectors representative of the geometric configuration of our synthetic database: (a) surface-normal vectors representing the topography, (b) source–station vectors representing the locations of sources relative to the locations of virtual receivers, and (c) histogram of the waves’ incidences to the free surface. Abscissas angles are equal to zero when the considered vector is vertical.

Khors-Sansorny, *et al.*, 2007) with a 10 m spatial discretization (i.e., more than 70 numerical cells per minimum wavelength; Bohlen and Saenger, 2006). Verification tests of our finite-difference method including topography were done by Maufroy (2010) through quantitative comparisons with the discontinuous Galerkin method introduced by Etienne *et al.* (2010). The tests revealed solution discrepancies smaller than 25% for frequencies below 4 Hz in most of the studied area (see fig. 4-3 of Maufroy, 2010). SHAKE3D simulates an infinite half-space by applying perfectly matched layer absorbing boundary conditions in every external limit of the computational domain and verifies the free-surface boundary conditions on top of the 3D model by applying the vacuum formalism (see Cruz-Atienza, 2006, and references therein). To isolate topographic site effects from others due to heterogeneities in the subsurface materials, we assumed, in all simulations, the same homogeneous linear elastic half-space (numerical box with dimensions  $5 \times 5 \times 7 \text{ km}^3$ ) with properties given by  $V_p = 5.0 \text{ km/s}$ ,  $V_s = 3.0 \text{ km/s}$ , and  $\rho = 2.6 \text{ g/cm}^3$ , for the  $P$ - and  $S$ -wave velocities and density, respectively. Supplementary details on the modeling procedure can be found in Maufroy *et al.* (2012).

The synthetic database counts on 200  $M_w$  4.5 double-couple point sources with a Gaussian-like time evolution, and for which focal mechanisms and locations were randomly generated beneath the area of interest (empty circles in Fig. 1b). An array of 576 receivers (black dots in Fig. 1b) is regularly spread over a  $2.5 \times 2.5 \text{ km}^2$  area that includes a diversity of topographic features such as valleys, slopes, and hills (Maufroy *et al.*, 2012). The average hypocentral distance computed at each receiver ranges from 5.1 to 5.7 km.

To assess how general our case study is in terms of diversity of seismic-ray azimuths and incidence angles at the free surface, we performed a geometrical analysis considering both surface-normal vectors at receiver locations and incident seismic-ray directions. Figure 2a shows the distribution of surface-normal vectors over the array. We find that most normal vectors have dipping angles smaller than  $40^\circ$

(i.e., terrain slopes not exceeding  $40^\circ$ ) and a wide range of azimuths with a tendency to the south ( $180^\circ$ ), which was expected because the studied area is located on the southern mountainside of the Albion plateau (Fig. 1).

Figure 2b presents the distribution of seismic-ray directions (i.e., source–receiver vectors) below the array and shows that sources cover the whole azimuthal range. In contrast, because we only considered local sources, the rays dipping angles cover from  $0^\circ$  (vertical rays) to  $60^\circ$ . By simply projecting the ray-direction vectors (Fig. 2b) into the surface-normal vectors (Fig. 2a), we can determine the wavefront incidence angles along the array considering the intricate topography. Results are shown in Figure 2c, in which we find that all incidence angles are lower than  $60^\circ$ , which means there is no grazing incidence in our case study. Although no cliff appears in the region, we estimate the geometric configuration behind our synthetic database covers a large variety of topographic features often present in real cases in which 3D site effects may occur.

### Analysis of Amplification Patterns

Following Maufroy *et al.* (2012), the topographic amplification over the stations’ array may be estimated by the median reference method (MRM) on each of the two horizontal components of ground motion. As described by these authors, the MRM quantifies the absolute amplification by assuming, as the reference level, the median ground motion in the area, sampled at the receiver’s positions, so that the critical choice of a reference site is avoided. The MRM is robust and accurate even within intricate topographic areas, where the site amplification is strongly dependent on frequency (Poppeliers and Pavlis, 2002; Maufroy *et al.*, 2012). In this work, we averaged the horizontal amplification factors such that, for a given frequency, we count on 200 amplification values per site, one for each earthquake. Because the seismic array has 576 receivers, our synthetic database integrates 115,200 amplification values per frequency that we study in the following from 1 to 4 Hz every 0.5 Hz.

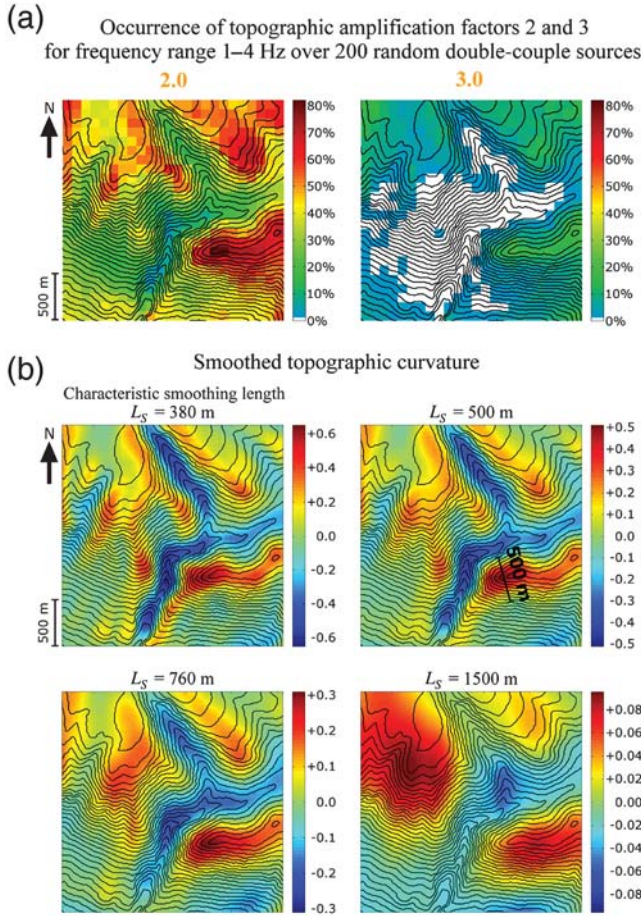


**Figure 3.** Maps of (a) occurrence of topographic amplification factors 2 and 3 in the 1–4 Hz frequency range over 200 random double-couple sources and (b) smoothed topographic curvature computed with four different characteristic smoothing lengths  $L_S$  ranging 380–1500 m. The individual topographic amplification factors are calculated with the median reference method (Maufroy *et al.*, 2012); the occurrence of amplification is given in percentage to reach a given factor on any component of the ground velocity and at any frequency between 1.0 and 4.0 Hz. White in (a) is for occurrence below 1.0%. The maps of curvature shown in (b) reveal the ridges (positive curvature, red) and the valleys (negative curvature, blue) at different length scales. Elevation contour lines are every 20 m.

Values reported per station and per frequency are the median of the 200 earthquakes population that we will call from now on median amplification factors (MAFs).

The topographic site effect is known to produce an amplification of the seismic waves that is strongly source dependent (Trifunac, 1972; Bouchon, 1973; Wong *et al.*, 1977). This can be seen in the work by Maufroy *et al.* (2012) for our database. Actually, the maximum ground-motion amplification generally occurs at crests on the opposite side of the upcoming wavefield, leading to a high-spatial variability of the amplification pattern that depends on both the topography and the hypocenter location. Thus, the pattern significantly differs from one simulation to another in our database. This is summarized in Figure 3a, in which we show

the probability of exceeding amplification factors 2 and 3 in the area (for any frequency between 1 and 4 Hz and for any of the three ground-motion components) as determined from our database using the MRM (see Maufroy *et al.*, 2012). Although very small in the deepest valleys (about 2%), there is nowhere that the probability of exceeding a factor 2 is zero. Besides, receivers located on crests or hills experience 50% and up to 80% probability of exceeding an amplification factor of 2. Regarding an amplification factor of 3, we find no probability in the lowest regions, whereas probabilities range from 10% on the hillsides (slopes) to 30% at the summits.

By simple inspection of the amplification patterns shown in Figure 3a (i.e., compare color map with topographic contour levels), it is clear that probabilities of exceedance correlate with the shape of the Earth’s surface (i.e., free surface curvature) rather than the elevation or slopes. For instance, we see that higher probabilities lie along convex spots (i.e., ridges), whereas lower probabilities lie over concave regions (i.e., valleys). In the following, we compare the amplification patterns with the topographic curvature, a metric that allows quantifying how concave or convex is the Earth’s surface.

### Estimation of the Topographic Curvature

Zevenbergen and Thorne (1987) introduced a method to estimate the topographic curvature along both downslope and across-slope directions. Following this method, the DEM of a region  $\mathbf{E}$  should be a rectangular matrix of evenly spaced elevation values with space increment  $h$ . The DEM curvature  $\mathbf{C}$  is thus defined as the second spatial derivative of matrix  $\mathbf{E}$  (the slope being defined as the first spatial derivative). To estimate  $\mathbf{C}$ , the method approximates function  $\mathbf{E}$  with a fourth-order polynomial (Zevenbergen and Thorne, 1987; Moore *et al.*, 1991) so that the curvature at any point  $(x_i, y_i)$  of matrix  $\mathbf{E}$  is given by

$$\mathbf{C}(x_i, y_i) = \mathbf{E}''(x_i, y_i) \approx -2(\delta + \varepsilon) \times 100, \quad (1)$$

in which  $\delta$  and  $\varepsilon$  are the fourth and fifth coefficients of the quadratic equation, which are approximated by finite differences as

$$\delta = \frac{1}{h^2} \left[ \frac{\mathbf{E}(x_{i-1}, y_i) + \mathbf{E}(x_{i+1}, y_i)}{2} - \mathbf{E}(x_i, y_i) \right] \quad (2)$$

and

$$\varepsilon = \frac{1}{h^2} \left[ \frac{\mathbf{E}(x_i, y_{i-1}) + \mathbf{E}(x_i, y_{i+1})}{2} - \mathbf{E}(x_i, y_i) \right]. \quad (3)$$

In these equations, the space increment  $h$  should be in the same units as the elevations in  $\mathbf{E}$  (e.g., meters in our case). The above procedure follows the work by Zevenbergen and Thorne (1987) and Moore *et al.* (1991) and allows topographic curvature estimates at any point of the DEM.

Topographic site effects for a given frequency are controlled by topographic features with characteristic sizes

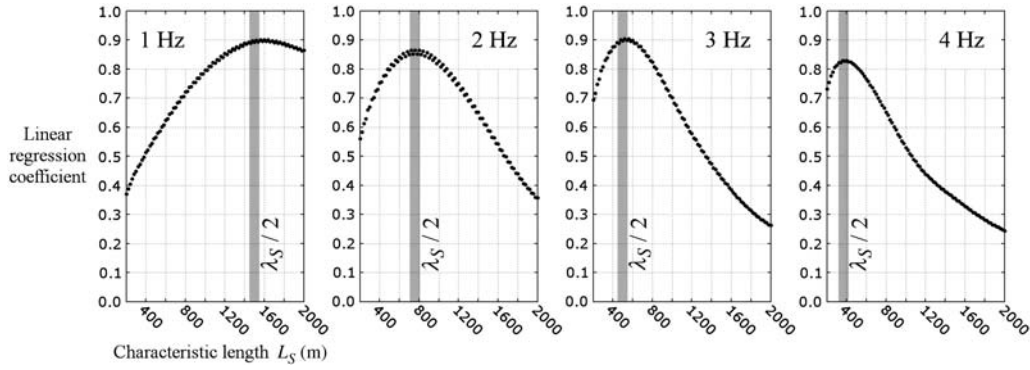


**Figure 4.** Linear regression coefficients obtained between the smoothed topographic curvature  $C_S$  and the median amplification factors (MAFs) over 200 sources at 576 sites (per site: one curvature value versus one median value of amplification) for different frequencies ranging 1–4 Hz. The linear regression coefficients are given related to the characteristic length  $L_S$  used to smooth the topographic curvature. The linear regression coefficients reach their highest values in each considered frequency when the curvature is two times smoothed and when the characteristic length  $L_S$  is equal to the  $S$  wavelength divided by two (as indicated by the vertical gray lines).

comparable with the associated wavelength (Geli *et al.*, 1988; Sánchez-Sesma and Campillo, 1991; Durand *et al.*, 1999; Buech *et al.*, 2010; Pischiutta *et al.*, 2010). The higher the frequency, the smaller are those features. Thus, to characterize the spatial correlation between topographic curvature and ground-motion amplification as a function of frequency, we introduce a smoothing operator over  $\mathbf{C}$ . The operator consists in a double convolution (one per derivative) of matrix  $\mathbf{C}$  with an  $n \times n$  unit matrix normalized by a factor  $n^4$  to preserve similar curvature estimates for any value of  $n$ . The smoothed curvature matrix is given by

$$C_S = \frac{1}{n^4} \left[ \mathbf{C} * \begin{pmatrix} 1_{11} & \cdots & 1_{1n} \\ \vdots & \ddots & \vdots \\ 1_{n1} & \cdots & 1_{nn} \end{pmatrix} * \begin{pmatrix} 1_{11} & \cdots & 1_{1n} \\ \vdots & \ddots & \vdots \\ 1_{n1} & \cdots & 1_{nn} \end{pmatrix} \right]. \quad (4)$$

The smoothing thus depends on the spatial extend of the unit matrix, which we define in meters by the characteristic length  $L_S = 2 \times n \times h$ . Because the convolution of two identical boxcar functions has a support twice as large as the function, the factor 2 must be considered to preserve the desired smoothing length. The larger  $L_S$  is,  $C_S$  is smoother. This can be seen in Figure 3b, in which we present topographic curvature estimates based on the 10 m resolution DEM of the i-DUST/LSBB area using four different values of  $L_S$  ranging from 380 to 1500 m. Positive values of  $C_S$  represent convex topographic features (e.g., ridges), whereas negative values correspond to concave features (e.g., valleys). Surface inflexions and flat regions are denoted by zero values. The curvature pattern for  $L_S = 380$  m highly correlates with the probability of exceeding amplification factor 2 (compare with left panel in Fig. 3a). From this exercise, it is clear that the characteristic length  $L_S$  will play a critical role in the determination of a frequency-dependent relationship between the topographic amplification and the surface curvature, as presented in the next section.

### Frequency-Dependent Relationship between Topographic Amplification and Curvature

A systematic linear regression analysis is performed to determine the relationship between the smoothed topographic curvature  $C_S$  (equation 4) and the MAFs along the seismic array. Linear regressions are done using MAFs from 200 sources per site in the 576-array stations at different frequencies between 1 and 4 Hz. On the other hand, smoothed curvature estimates at each station  $C_S$  are computed for a large range of characteristic length  $L_S$  (i.e., between 200 and 2000 m). Results from the linear regressions are shown in Figure 4, in which we present (for different frequencies) the corresponding coefficients in the entire array as a function of  $L_S$ . Two main observations detach from this exercise: (1) regression coefficient curves show a single and well-defined maximum at different values of  $L_S$  and (2)  $L_S$  values at the maxima depend on frequency and coincide with half the wavelength of the  $S$  waves  $\lambda_S$  (i.e.,  $L_S = \lambda_S/2 = V_S/2f$ , in which  $V_S = 3$  km/s in our case study; see gray bands). For instance, at 2 Hz, the maximum appears at  $L_S = 750$  m and  $\lambda_S/2 = 3000/4 = 750$  m. A similar analysis was done computing  $C_S$  values with only one smoothing (i.e., by convolving only once matrix  $\mathbf{C}$  with the  $n \times n$  unit matrix, see equation 4), confirming no clear correlation between the maxima and  $\lambda_S$  (results not shown). Indeed the convolution is required to smooth the derivative at the scale of interest, but it must be carried out each time a derivative is performed (i.e., a double convolution to smooth the second derivative of the DEM).

Figure 5a shows MAF estimates along the array as a function of  $C_S$  for the same four frequencies. For each frequency, the characteristic length  $L_S$  used to smooth the topographic curvature is indicated in each panel and is equal to  $\lambda_S/2$  (i.e., the characteristic length that maximizes the linear regression coefficients). Note that small curvature values ( $C_S \approx 0$ , i.e., flat topographic regions) correspond to almost no amplification (MAF  $\approx 1$ ). Although correlation between amplification

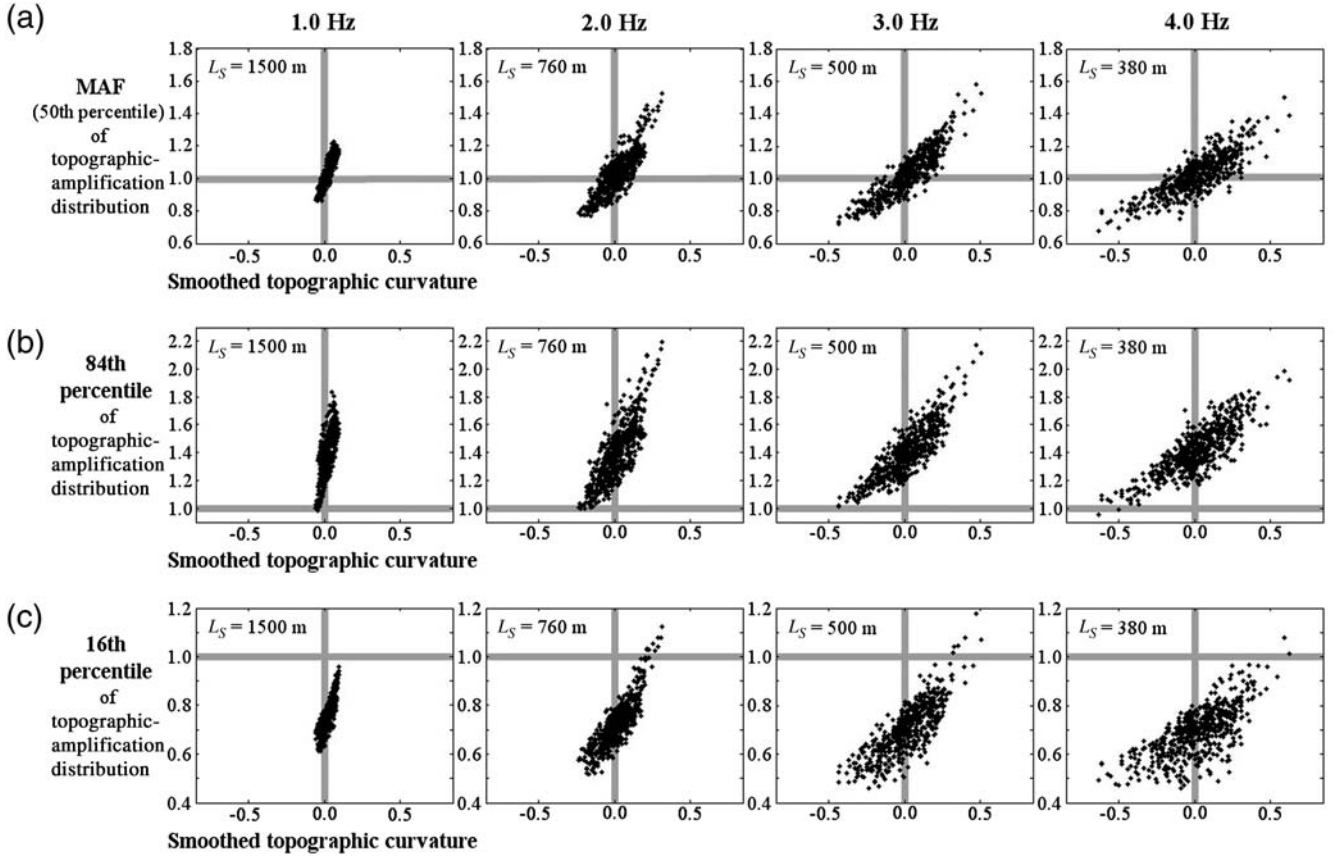


**Figure 5.** Correlation between the smoothed topographic curvature and (a) the median value (50th percentile) of the horizontal topographic-amplification distribution over 200 sources at 576 sites (per site: one curvature value versus one median value of amplification), (b) the 84th percentile of that same distribution of amplification factors, (c) the 16th percentile. The correlation is shown for different frequencies ranging 1–4 Hz. The characteristic length  $L_S$  to smooth the curvature at each frequency is chosen as the  $S$  wavelength divided by two. The vertical gray lines indicate the level 0 of curvature (corresponding to flat surface or regular slope). The horizontal gray lines indicate the amplification factor 1.0 (i.e., no amplification or deamplification). (a) The level 0 of curvature correlates with a median value of topographic-amplification distribution equal to one.

factors and curvature is high, the dataset clearly shows some dispersion. This means that MAFs may significantly differ between sites with similar topographic curvatures.

A closer analysis of the amplification distribution reveals the 84th percentile (the MAF being the 50th percentile) also correlates with  $L_S$  (Fig. 5b) and corresponds to amplification factors larger than one, even at topographic concave sites such as valleys (i.e., with negative curvature values). In contrast, the 16th percentile of the amplification distribution mainly corresponds to amplification factors smaller than one (i.e., deamplification, Fig. 5c), even in convex sites such as ridges and summits (i.e., with positive curvature values). Thus, Figure 5b,c clearly shows the extent of the variability of topographic site effects. Although the probability of occurrence is low, amplification can happen in valleys and deamplification in ridges and summits. In a given site, this will depend on the location and mechanism of the source. The variability of the topographic site effects will be further analyzed in the next section.

From Figures 4 and 5, we conclude that there is a linear correlation between site effects and the topographic curva-

ture. It is also clear that such correlation is frequency dependent because  $C_S$  depends on the  $S$  wavelength  $\lambda_S$  through the characteristic smoothing length  $L_S(f) = \lambda_S/2 = V_S/2f$ , so that the correlation may be expressed in the following terms:

$$\text{MAF}(f) = \alpha \times C_S(L_S) + \beta. \quad (5)$$

Figure 5 further shows that MAF frequency dependence also comes from coefficient  $\alpha(f)$ , which is inversely proportional to  $f$  and thus proportional to  $\lambda_S$ . After a linear regression analysis for  $\alpha$  and  $\lambda_S$  (with high regression coefficient  $R^2 = 0.997$ ), we found  $\alpha = 0.0008 \times \lambda_S$ . Regarding the intercept coefficient  $\beta$  in equation (5) we also see, from Figure 5, that MAFs are close to one for small topographic curvatures (i.e.,  $C_S \approx 0$ ), whatever the frequency is in the studied range. Therefore, equation (5) may be written as

$$\text{MAF}(f) = (0.0008 \times \lambda_S) \times C_S(L_S) + 1. \quad (6)$$

Following the same procedure for the 84th and 16th percentiles shown in Figure 5b,c, linear regressions for

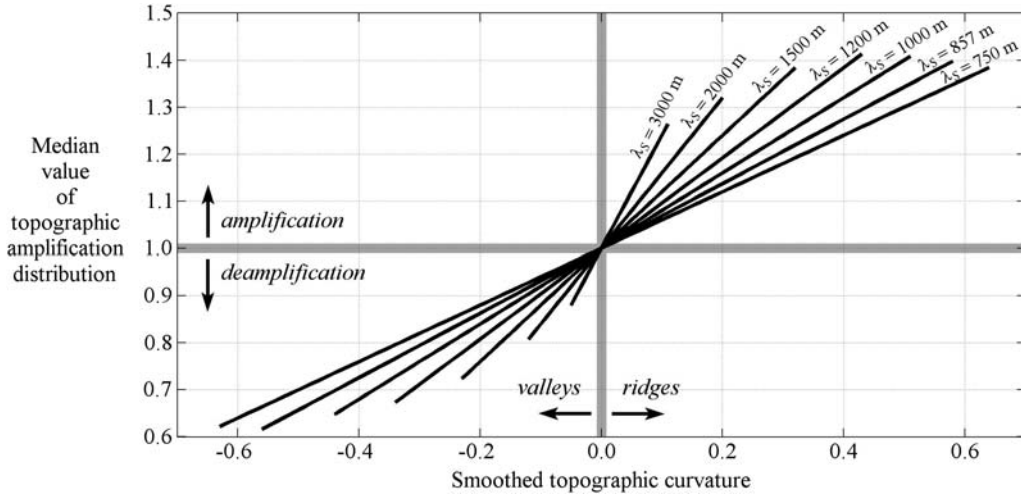


**Figure 6.** Linear relation established between the smoothed topographic curvature and the median value of the topographic-amplification distribution following equation (6). This linear relation is dependent on the considered  $S$  wavelength, as it is shown for  $S$  wavelengths ranging 750–3000 m. The wavelength-dependent relations are not displayed outside the limits of this study (i.e., each line is plotted only between the minimum and maximum values of curvature obtained in our case study for the corresponding wavelength). The vertical gray line indicates the level 0 of curvature separating valleys from ridges, whereas the horizontal gray line indicates the amplification factor 1.0 separating amplification from deamplification.

coefficients  $\alpha$  yielded  $R^2 > 0.99$  in both cases, and the corresponding relationships:  $\alpha_{84\text{th}} = 0.0012 \times \lambda_S - 0.1$  and  $\alpha_{16\text{th}} = 0.0007 \times \lambda_S - 0.1$ . Regarding the intercepts, we got  $\beta_{84\text{th}} = 1.4$  and  $\beta_{16\text{th}} = 0.7$ . Thus, from equation (5) we finally obtain

$$\text{AF}_{84\text{th}}(f) = (0.0012 \times \lambda_S - 0.1) \times C_S(L_S) + 1.4, \quad (7)$$

$$\text{AF}_{16\text{th}}(f) = (0.0007 \times \lambda_S - 0.1) \times C_S(L_S) + 0.7. \quad (8)$$

To exactly center the smoothing window on a given site, the value of  $n$  (equation 4) has to be an odd number equal to or greater than 3. For each value of  $n$ , the corresponding  $S$  wavelength is defined by  $\lambda_S = 2L_S = 4 \times n \times h$ . Because  $n$  takes odd discrete values (3, 5, 7, ...), the curvature  $C_S$  and therefore the predicted amplification are computed only at discrete values of  $S$  wavelengths increasing by  $8h$  (12h, 20h, 28h...). This restriction is not critical when using high-resolution DEM.

MAFs predicted by equation (6) for different  $S$  wavelengths are shown in Figure 6. Chosen values of  $\lambda_S$  correspond to frequencies from 1 to 4 Hz every 0.5 Hz. The theoretical MAFs displayed in this figure are constrained to the limits of this study, so each line is plotted between the minimum and maximum values of  $C_S$  found in our topographic domain. We find two separate domains in the plot: one for negative curvatures and deamplifications, which correspond to sites located in valleys, and another for positive curvatures and amplifications, which include sites on ridges and summits. We recall that equation (6) predicts median values determined from our 200 sources population, so larger

amplification factors than those in the figure actually happen in the region, as suggested in Figure 3a and clearly shown later in Figure 7.

The largest MAFs in the studied area are found for intermediate wavelengths, around 1000 and 1200 m (i.e., 3.0 and 2.5 Hz). We also see that, to reach the same amplification level, smaller wavelengths require larger curvatures (i.e., sharper topographic features). Although our synthetic database prevents us from observing site-effect patterns for  $S$  wavelengths smaller than 750 m, assuming that the topographic amplification behaves linearly beyond the limits of the study as suggested in Figure 6, we estimate that curvature values larger than 1 are required to produce some moderate amplification at the highest frequencies. As an example, for  $S$  wavelengths of 280 m (i.e., 10.7 Hz in our case study), the theoretical MAF only reaches 1.36 at the maximum curvature of 1.6 found in a small  $50 \times 50 \text{ m}^2$  area of our topographic domain.

Predictions of the 84th and 16th percentiles from equations (7) and (8) (dashed lines) are plotted in Figure 7 along with the predicted MAFs (solid lines, equation 6) for different frequencies. The figure also includes the whole distribution of horizontal amplification factors (light gray dots) and the associated MAF at all receivers (dark gray dots). Note the good agreement, for all frequencies, between the actual MAF values and their prediction yielded by equation (6) (solid lines). Furthermore, we also see that predictions of MAFs based on linear regression models are not enough to embrace the variability of ground motions due to the interaction of topography with the incoming wavefield (i.e., compare median values in dark gray dots with the overall maximum of the actual amplification factors in light gray dots). To better understand this phenomenon and thus to improve

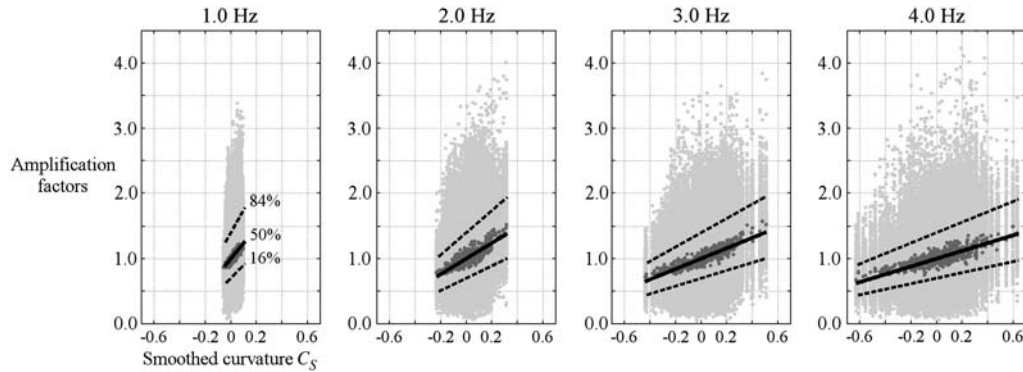


**Figure 7.** Distribution of all topographic amplification factors at 576 sites for 200 sources (light gray dots; individually computed from the average of both horizontal factors) in relation with the smoothed topographic curvature  $C_S$  for various frequencies ranging 1–4 Hz. The MAFs obtained at each receiver over the 200 sources are superimposed as darker dots. The best-fitting linear relations for the MAF (solid black line) and for percentiles 16% and 84% (dashed black lines) are shown to characterize the distribution obtained in each frequency.

its prediction, it is essential to characterize the extent of such variability and its relationship with the topography. We address this issue in the following section.

### Effects of Topography on Ground-Motion Variability

Our synthetic database offers a unique opportunity to investigate, in detail, the variability of ground motion due to the topography at every single station. To this purpose we computed, from our 200 random-source scenarios, the spatial distribution of the median peak ground acceleration (PGA) in the horizontal components (Fig. 8a) and the associated PGA variability  $\sigma_S$  computed at each station (Fig. 8d). Estimates correspond to a maximum frequency of 4 Hz. Two main observations emerge: (1) there is a clear correlation between median PGA and the amplification pattern at 4 Hz predicted by equation (6) (compare Fig. 8a and b) and (2) the PGA variability (i.e., standard deviations  $\sigma_S$ ) is significantly lower in the valleys (Fig. 8d). This means that PGA also correlates with  $C_S$ , the smoothed topographic curvature, as shown in Figure 8c for wavelengths at 4 Hz (i.e.,  $L_S = \lambda_S/2 \approx 380$  m). However, although PGA variability  $\sigma_S$  tends to be smaller in concave topographic regions (i.e., negative  $C_S$  values; see Fig. 8e), the variability pattern is substantially more complex; for a given curvature value, we find variations of  $\sigma_S$  up to  $\sim 30\%$  and relatively small variability of ground motions along certain convex spots with high curvatures such as those indicated with a red circle. A linear correlation analysis between  $C_S$  and  $\sigma_S$  is not reasonable (Fig. 8e), even for the characteristic smoothing length  $L_S = 760$  m that maximizes the correlation coefficient in this case (not shown).

Figure 9a shows the distribution of the 576 median PGA values (those of Fig. 8a). Dividing these values by the MAF predictions (equation 6 and Fig. 8b) at the maximum resolved frequency (i.e., 4 Hz) would statistically remove most of the topographic site effect from the median PGAs. The result of this procedure is shown in Figure 9b, in which we plot PGA values after removing the site-effect amplification. This illustrates how integrating the topographic curvature

into this ground-motion model reduces the dispersion of the 576 median PGA values (i.e., standard deviation reduction from 0.049 to 0.025). At the same time, this procedure has little impact on the  $\sigma_S$  values and therefore on the overall ground-motion variability (sigma) of the entire database. Actually, the reduction of the overall sigma ( $\sigma$ ) is very modest (from 0.224 to 0.221). This is consistent with previous works (e.g., Strasser *et al.*, 2009), in which integrating site-effect terms into ground-motion models does not necessarily lead to a better description of the ground-motion variability.

Figure 10 shows the distribution of PGA variabilities ( $\sigma_S$ ) along the array. Interesting observations detach from this distribution and from the corresponding map in Figure 8d associated to Figure 8e. The largest PGA variabilities are found at sites located on slopes and on the largest summits. We define a large summit as a large, almost flat summit bounded by upper slopes including perched valleys. One hypothesis that may explain such variabilities on large summits is a higher dependence on the source–site configuration. One site located on a large summit may not be affected by the slopes and crests surrounding the summit because of its extension: depending on the direction of the upcoming wavefield, the site may or may not experience topographic amplification. It may also occur that the roughness of the upper slopes including inner valleys can strongly disrupt the amplification pattern. In contrast, narrow ridges, which are defined as thin topographic features with steep slopes facing all directions, experience an intermediate level of variability: whatever the source–site configuration is, these regions frequently show large ground motions. Finally, bottom valleys present a stable behavior (i.e., small variability) and low ground motions. These results show that understanding the physical reasons for ground-motion variability deserves further analysis and that the variability is not only due to topography but also to source–site interactions.

Although the topographic curvature alone may not completely explain the variability of ground motions at single sites, amplification factor regressions for the 16th and



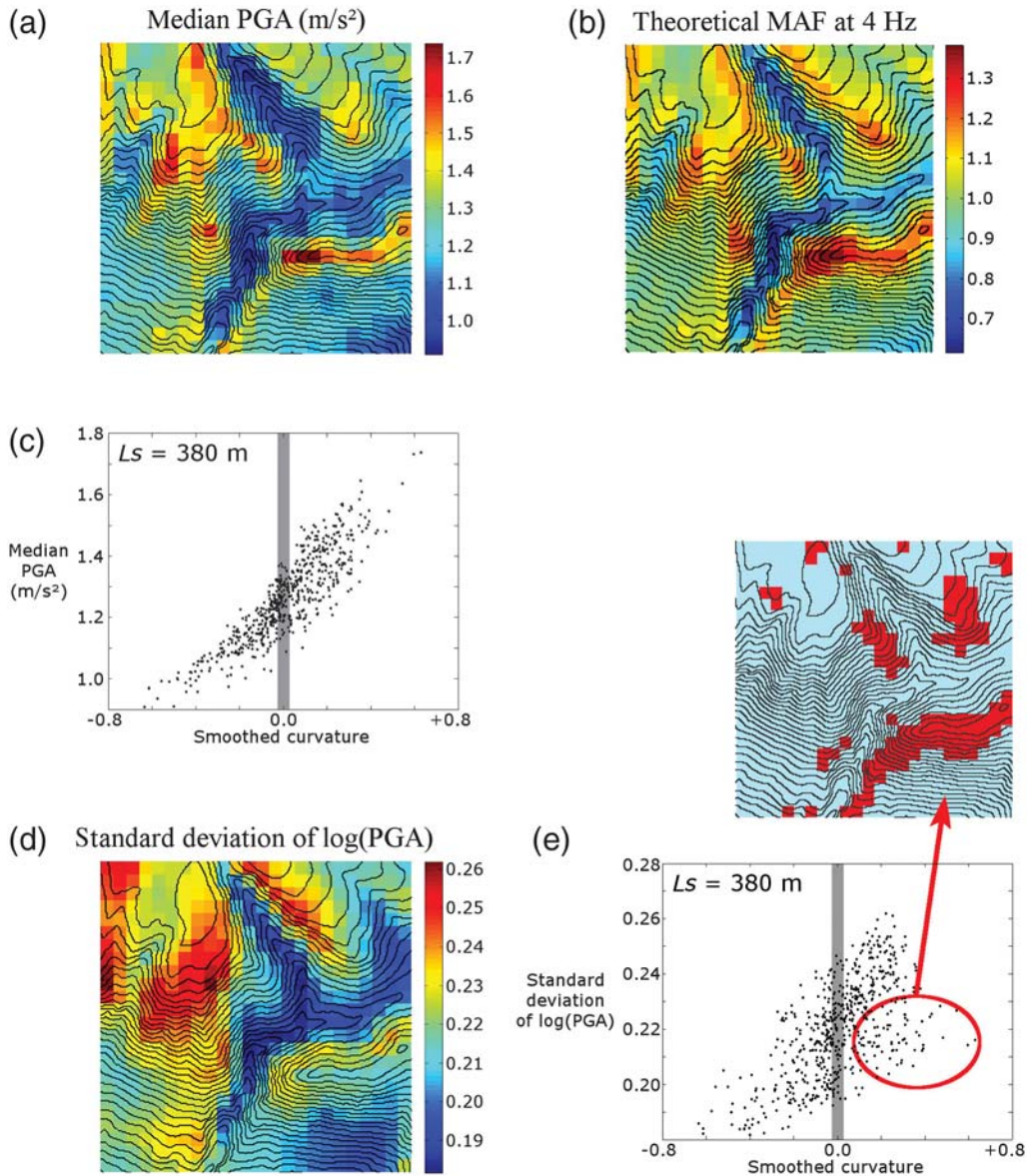


**Figure 8.** (a) Median peak ground acceleration (PGA) obtained from our synthetic database, (b) theoretical MAFs estimated at 4 Hz following equation (6), (c) best-fitting linear correlation of the median PGA with the smoothed topographic curvature reached for a characteristic smoothing length  $L_S = 380$  m, (d) standard deviation of  $\log(\text{PGA})$  obtained from our synthetic database, and (e) linear correlation of the standard deviation of  $\log(\text{PGA})$  with the smoothed curvature for a characteristic smoothing length  $L_S = 380$  m. The bold vertical gray lines indicate the level 0 of curvature separating valleys from ridges. As pointed out by the red circle in (e), the spatial locations of sites showing high curvature and relatively lower values of standard deviation of  $\log(\text{PGA})$  are shown in red in the inserted map. Individual values of PGA are computed from the average of absolute peak values on the two horizontal components of ground acceleration.

84th percentiles (equations 7 and 8) satisfactorily capture the frequency-dependent variability in most cases. Figure 11 shows predicted (solid and dashed lines, right panels) and actual (open circles) horizontal amplification factors as a function of the  $S$  wavelength at five selected sites, along with the associated estimates of the topographic curvature,  $C_S$  (left panels). The figure also shows individual amplification factors from the whole database (light gray dots). The sites lie on different topographic features (i.e., those indicated in Fig. 10) such as summits with different sharpness and the deepest valley. Both median and percentile predictions by

equations (6)–(8) encompass satisfactorily well the corresponding data-based values, except at the narrow ridge site where we find the largest misfit in the whole topographic domain with underestimations of about 30%. Actual misfits come from the linear regressions assumed in this study that cannot explain the data scattering (e.g., compare solid lines and dark gray dots in Fig. 7). The scattering tends to grow with frequency (Fig. 5) and may be due to different factors, such as (1) uncertainties in the amplification-factor estimates by the MRM (Maufroy *et al.*, 2012), (2) uncertainties in the curvature computation related to the DEM resolution, and

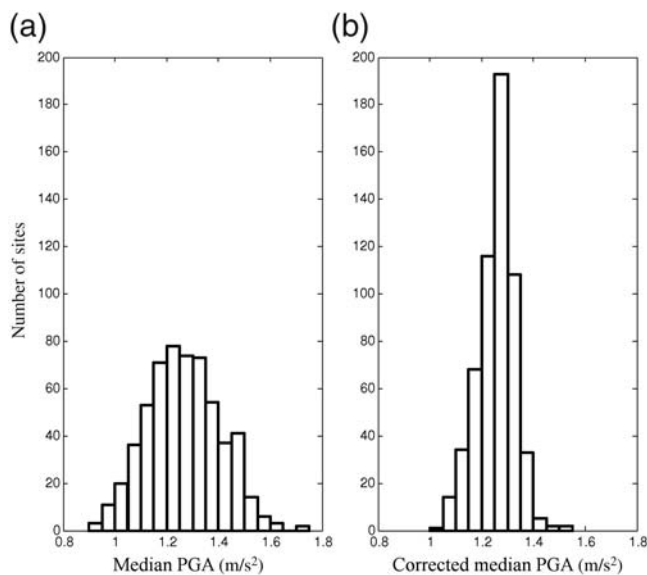


**Figure 9.** (a) Distribution of the 576 median PGA observed in our synthetic database (one value per virtual receiver) and (b) distribution of the same data after correction of the median topographic amplification predicted by equation (6) at 4 Hz (maximum frequency of the synthetic ground motion). Bin size for both panels is 0.05 Hz.

(3) inaccuracies in the ground-motion simulations (Maufroy, 2010), among others. To minimize their effects, we considered: (1) several hundreds of receivers, (2) a 10 m DEM, and (3) more than 70 numerical cells per minimum wavelength. Even though the uncertainties are small, their cumulative effect increases with frequency, producing scattered estimates. Thus, the maximum 30% error yielded by our frequency-scaled curvature (FSC) proxy (i.e., by our topographic-amplification prediction equations 6–8) must be considered when estimating variation ranges of topographic site effects in a given region.

The topographic diversity of the selected sites shown in Figure 11 may be quantified through function  $C_S$  (left panels) used to generate the amplification-factor predictions. The large summit and narrow ridge sites present curvature functions with only positive values, which imply median amplifications at all considered wavelengths (see right panels). In contrast, the bottom valley site presents a curvature function with only negative values, which implies topographic deamplifications. The  $C_S$  function at the slope site looks more complex but has small values, and thus there is almost no topographic effect. The perched valley site shows an interesting behavior; for short wavelengths the curvature values are negative, producing a small deamplification associated to the geometry of the local narrow valley, whereas at longer wavelengths, the curvature becomes positive, leading to topographic amplification associated to the large summit where the valley is located. This analysis shows the FSC proxy is a powerful tool to characterize the frequency-dependent topographic site effect along with probabilistic estimates of its variability.

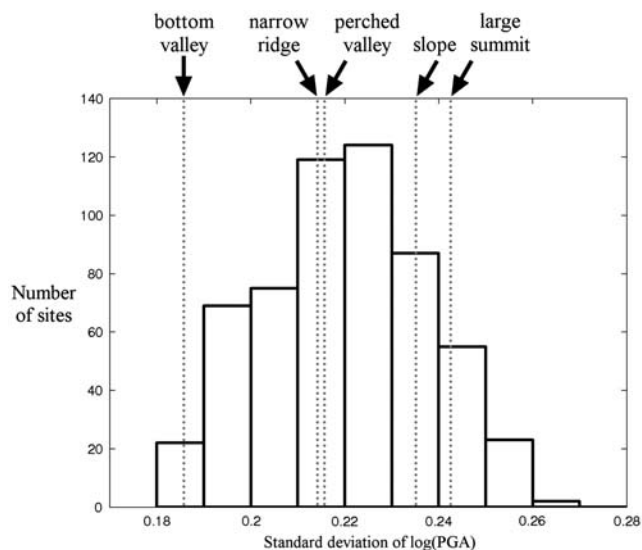


**Figure 10.** Distribution of the standard deviation of  $\log(\text{PGA})$  observed in our synthetic database (one value per virtual receiver; map shown in Fig. 8d). The values of five particular sites are marked on the histogram; the location of these sites is shown in Figure 11.

## Discussion

The FSC proxy, as defined in this work, allows predicting statistical values of the topographic amplification factors as a function of frequency, which is particularly useful in regions where source locations and mechanisms are variable. However, topographic-amplification prediction for a specific source scenario deserves a deeper understanding of the source–site interaction from a statistical viewpoint to avoid expensive 3D numerical simulations.

Regarding the topographic-amplification prediction equations (6)–(8) proposed in this study, one should be aware that (1) they predict median values (equation 6), the 84th percentile (equation 7) is more representative of the high level of amplification expected at specific sites; (2) predictions correspond to the average of both horizontal components, which means the amplification factor may differ from one component to the other (Massa *et al.*, 2014); and (3) the topographic steepness of the i-DUST/LSBB study area is not extreme (i.e., slopes smaller than  $40^\circ$ ), so one should expect higher levels of amplification on steeper topographies as compared to those reported in this study.

Because we could not establish a clear correlation between  $C_S$  and the amplification on both separate horizontal components of the ground motion, in this work we defined the amplification as the average. Topographic-amplification partitioning on both horizontal components is not yet clearly understood, though some insights have already been proposed (Bouchon and Barker, 1996; Spudich *et al.*, 1996; Del Gaudio and Wasowski, 2007; Massa *et al.*, 2010, 2014). Thus, the FSC proxy is not able to predict extreme directional effects and then to distinguish, for instance,

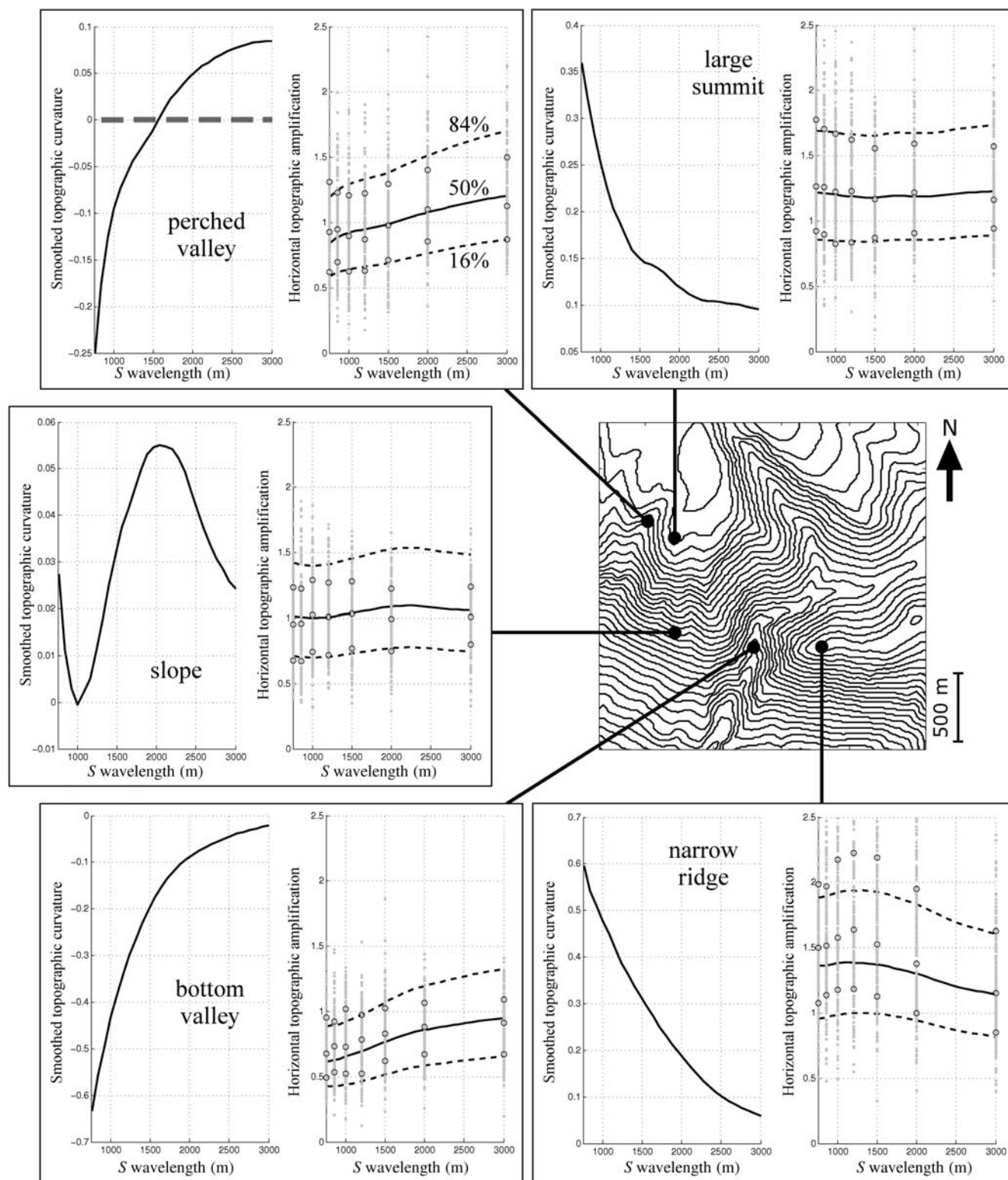


**Figure 11.** Profiles of smoothed topographic curvature and horizontal topographic amplification, both related to  $S$  wavelength, for five particular sites in the i-DUST/LSBB area. The predicted median (solid line, equation 6) and percentiles (16% and 84%, dashed lines; equations 7 and 8) of topographic amplification are superimposed on the values observed in our synthetic database (empty circles) and on the individual amplification factors (light gray dots) shown for selected  $S$  wavelengths.

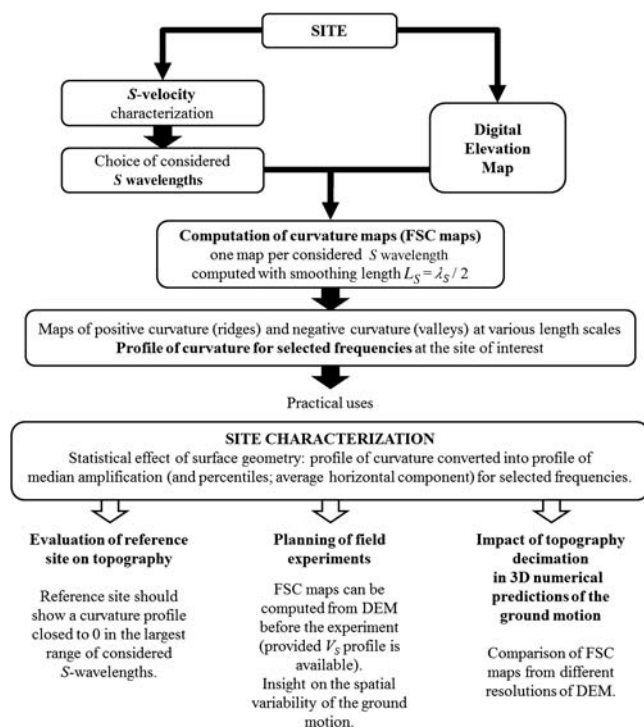


**Figure 12.** Flowchart showing the potential practical uses of the frequency-scaled curvature proxy, provided that both digital elevation map and characterization of consistent  $S$  velocity are available at the site of interest.

whether amplification occurs on one component as deamplification occurs on the other.

The topographic curvature is easily computed from the DEM. However, because the topographic site effect is sensitive to local wavelengths, to gain confidence in the amplification factors produced by the FSC proxy, some knowledge of the elastic properties in the studied region is required. Our numerical study is performed in a homogeneous medium, which is useful to isolate the geometric effect of topography on ground motions from other case-dependent effects due to the near-surface geology. The FSC proxy is thus useful in many regions where little or no information exists about the local geology and possible consequences of the ground shaking (i.e., landslides), providing a quantitative way to generate physical estimates (and reasonable variation ranges) for engineering purposes in mountainous regions. Yet, to investigate the amplification level, in detail, accounting on possible coupled effects due to both the local velocity structure and topography (Assimaki and Jeong, 2013; Burjánek *et al.*, 2014; Massa *et al.*, 2014), complementary on-field and numerical studies are convenient.

To perform a detailed analysis of site response in a given region, we thus propose the flowchart shown in Figure 12, which summarizes the procedure that we have introduced to statistically predict the effect of topography on the ground motion using the FSC proxy at given sites of interest and for selected frequencies. The procedure starts with the availability of the DEM and with the characterization of the

$S$ -velocity structure. The procedure ends with some examples of practical applications of the FSC proxy. If its main application remains the site-effect estimation, this tool could provide some secondary uses such as evaluating the reference stations at rock sites, planning the spatial distribution of receivers in field experiments, or estimating the accuracy required for the surface representation in 3D numerical simulations of the ground motion.

## Conclusions

We have introduced a new methodology to predict the topographic site-effect amplification based on the Earth's surface curvature, defined as the second spatial derivative of the surface elevation map. Ground motions obtained from a large database of 3D earthquake simulations show the topographic curvature is correlated with the topographic amplification. The highest linear correlation between the frequency-dependent amplification and the FSC is reached when the curvature is smoothed over a characteristic length equal to half of the  $S$  wavelength. This implies, for a given frequency, the amplification is caused by topographic features with horizontal dimensions that are similar to that length. We showed that applying an adaptive smoothing operator to the topographic curvature computed as proposed by Zevenbergen and Thorne (1987) and Moore *et al.* (1991) is a powerful means to precisely determine topographic features sensitive to the same wavelength.

The FSC proxy allows the estimation of statistical values of the topographic amplification through a set of prediction equations that take into account the variability of the site effect. Indeed the largest ground-motion variabilities are found at sites located on slopes and on the largest summits. One hypothesis explaining these variabilities is a higher dependence of those topographic features on the source–site configuration. In contrast, narrow ridges exhibit intermediate levels of variability, whereas the bottom valleys show more stable behavior.

No high-performance computing is required for the curvature computation. The topographic-amplification estimates from the FSC proxy are robust and easily obtained from DEMs provided reasonable values of the  $S$ -wave velocities in the area of interest.

## Data and Resources

This work was granted access to the High Performance Computer (HPC) resources of Institut du Développement et des Ressources en Informatique Scientifique (IDRIS) under the allocation i2009046038 made by Grand Equipement National de Calcul Intensif (GENCI). The digitalization of the topography surrounding the inter-Disciplinary Underground Science and Technology Laboratory (i-DUST/LSBB, Rustrel, France) was provided by the Institut National de l'Information Géographique et Forestière (IGN), France.

## Acknowledgments

We are thankful to Adrian Rodriguez-Marek and Manisha Rai from the Virginia Polytechnic Institute and State University (Virginia Tech, Blacksburg, Virginia) and to Emmanuel Chaljub, Pierre-Yves Bard, and Robin Gee from ISTERre, University of Grenoble Alpes (France) for constructive and helpful discussions. We deeply thank Florent De Martin from Bureau des Recherches Géologiques et Minières (BRGM, France) and an anonymous reviewer for their interesting and thorough review of this work. Emeline Maufroy gratefully acknowledges financial support from the Cashima project.

## References

- Ashford, S. A., N. Sitar, J. Lysmer, and N. Deng (1997). Topographic effects on the seismic response of steep slopes, *Bull. Seismol. Soc. Am.* **87**, no. 2, 701–709.
- Assimaki, D., and S. Jeong (2013). Ground-motion observations at Hotel Montana during the M 7.0 2010 Haiti earthquake: Topography or soil amplification? *Bull. Seismol. Soc. Am.* **103**, no. 5, 2577–2590, doi: [10.1785/0120120242](https://doi.org/10.1785/0120120242).
- Assimaki, D., G. Gazetas, and E. Kausel (2005). Effects of local soil conditions on the topographic aggravation of seismic motion: Parametric investigation and recorded field evidence from the 1999 Athens earthquake, *Bull. Seismol. Soc. Am.* **95**, no. 3, 1059–1089, doi: [10.1785/0120040055](https://doi.org/10.1785/0120040055).
- Assimaki, D., E. Kausel, and G. Gazetas (2005). Soil-dependent topographic effects: A case study from the 1999 Athens earthquake, *Earthq. Spectra* **21**, no. 4, 929–966, doi: [10.1193/1.2068135](https://doi.org/10.1193/1.2068135).
- Bohlen, T., and E. H. Saenger (2006). Accuracy of heterogeneous staggered-grid finite-difference modeling of Rayleigh waves, *Geophysics* **71**, no. 4, T109–T115, doi: [10.1190/1.2213051](https://doi.org/10.1190/1.2213051).
- Bommer, J. J., and N. A. Abrahamson (2006). Why do modern probabilistic seismic-hazard analyses often lead to increased hazard estimates? *Bull. Seismol. Soc. Am.* **96**, no. 6, 1967–1977, doi: [10.1785/0120060043](https://doi.org/10.1785/0120060043).
- Boore, D. M. (1973). The effect of simple topography on seismic waves: Implications for the accelerations recorded at Pacoima Dam, San Fernando Valley, California, *Bull. Seismol. Soc. Am.* **63**, no. 5, 1603–1609.
- Bouchon, M. (1973). Effect of topography on surface motion, *Bull. Seismol. Soc. Am.* **63**, no. 2, 615–632.
- Bouchon, M., and J. S. Barker (1996). Seismic response of a hill: The example of Tarzana, California, *Bull. Seismol. Soc. Am.* **86**, no. 1A, 66–72.
- Bouckovalas, G. D., and A. G. Papadimitriou (2005). Numerical evaluation of slope topography effects on seismic ground motion, *Soil Dynam. Earthq. Eng.* **25**, 547–558, doi: [10.1016/j.soildyn.2004.11.008](https://doi.org/10.1016/j.soildyn.2004.11.008).
- Buech, F., T. R. Davies, and J. R. Pettinga (2010). The Little Red hill seismic experimental study: Topographic effects on ground motion at a bedrock-dominated mountain edifice, *Bull. Seismol. Soc. Am.* **100**, no. 5A, 2219–2229, doi: [10.1785/0120090345](https://doi.org/10.1785/0120090345).
- Burjánek, J., B. Edwards, and D. Fäh (2014). Empirical evidence of local seismic effects at sites with pronounced topography: A systematic approach, *Geophys. J. Int.* **197**, no. 1, 608–619, doi: [10.1093/gji/ggu014](https://doi.org/10.1093/gji/ggu014).
- Çelebi, M. (1987). Topographical and geological amplifications determined from strong-motion and aftershocks records of the 3 March 1985 Chile earthquake, *Bull. Seismol. Soc. Am.* **77**, no. 4, 1147–1167.
- Chaljub, E., P. Moczo, S. Tsuno, P.-Y. Bard, J. Kristek, M. Käser, M. Stupazzini, and M. Kristeková (2010). Quantitative comparison of four numerical predictions of 3D ground motion in the Grenoble valley, France, *Bull. Seismol. Soc. Am.* **100**, no. 4, 1427–1455, doi: [10.1785/0120090052](https://doi.org/10.1785/0120090052).
- Cruz-Atienza, V. M. (2006). Rupture dynamique des failles non-planaires en différences finies, *Ph.D. Thesis*, University of Nice-Sophia Antipolis, France.
- Cruz-Atienza, V. M., J. Virieux, and H. Aochi (2007). 3D finite-difference dynamic-rupture modeling along non-planar faults, *Geophysics* **72**, no. 5, SM123–SM137, doi: [10.1190/1.2766756](https://doi.org/10.1190/1.2766756).
- Cruz-Atienza, V. M., J. Virieux, C. Khors-Sansorny, O. Sardou, S. Gaffet, and M. Vallée (2007). Estimation quantitative du PGA sur la Côte d’Azur, *7ème Colloque National*, Association Française du Génie Parasismique (AFPS), Ecole Centrale Paris, France, 8.
- De Martin, F., S. Matsushima, and H. Kawase (2013). Impact of geometric effects on near-surface Green’s functions, *Bull. Seismol. Soc. Am.* **103**, no. 6, 3289–3304, doi: [10.1785/0120130039](https://doi.org/10.1785/0120130039).
- Del Gaudio, V., and J. Wasowski (2007). Directivity of slope dynamic response to seismic shaking, *Geophys. Res. Lett.* **34**, L12301, doi: [10.1029/2007GL029842](https://doi.org/10.1029/2007GL029842).
- Durand, S., S. Gaffet, and J. Virieux (1999). Seismic diffracted waves from topography using 3-D discrete wavenumber-boundary integral equation simulation, *Geophysics* **64**, no. 2, 572–578, doi: [10.1190/1.1444564](https://doi.org/10.1190/1.1444564).
- Etienne, V., E. Chaljub, J. Virieux, and N. Glinesky (2010). An hp-adaptive discontinuous Galerkin finite-element method for 3-D elastic wave modelling, *Geophys. J. Int.* **183**, no. 2, 941–962, doi: [10.1111/j.1365-246X.2010.04764.x](https://doi.org/10.1111/j.1365-246X.2010.04764.x).
- Gaffet, S., G. Cultrera, M. Dietrich, F. Courboulex, F. Marra, M. Bouchon, A. Caserta, C. Cornou, A. Deschamps, J.-P. Glot, and R. Guiguet (2000). A site effect study in the Verchiano valley during the 1997 Umbria-Marche (Central Italy) earthquakes, *J. Seismol.* **4**, no. 4, 525–541.
- Geli, L., P.-Y. Bard, and B. Jullien (1988). The effect of topography on earthquake ground motion: A review and new results, *Bull. Seismol. Soc. Am.* **78**, no. 1, 42–63.
- Hough, S. E., J.-R. Altidor, D. Anglade, D. Given, M. Guillard Janvier, J. Zebulon Maharrey, M. Meremonte, M. Bernard Saint-Louis, C. Prepetit, and A. Yong (2010). Localized damage caused by topographic amplification during the 2010 M7.0 Haiti earthquake, *Nat. Geosci.* **3**, no. 11, 778–782, doi: [10.1038/ngeo988](https://doi.org/10.1038/ngeo988).
- Kawase, H., and K. Aki (1990). Topography effect at the critical SV-wave incidence: Possible explanation of damage pattern by the Whittier Narrows, California, earthquake of 1 October 1987, *Bull. Seismol. Soc. Am.* **80**, no. 1, 1–22.
- Lee, S.-J., Y.-C. Chan, D. Komatitsch, B.-S. Huang, and J. Tromp (2009). Effects of realistic surface topography on seismic ground motion in the Yangminshan region of Taiwan based upon the spectral-element method and LiDAR DTM, *Bull. Seismol. Soc. Am.* **99**, no. 2A, 681–693, doi: [10.1785/0120080264](https://doi.org/10.1785/0120080264).
- Lee, S.-J., D. Komatitsch, B.-S. Huang, and J. Tromp (2009). Effects of topography on seismic-wave propagation: An example from northern Taiwan, *Bull. Seismol. Soc. Am.* **99**, no. 1, 314–325, doi: [10.1785/0120080020](https://doi.org/10.1785/0120080020).
- Massa, M., S. Barani, and S. Lovati (2014). Overview of topographic effects based on experimental observations: Meaning, causes and possible interpretations, *Geophys. J. Int.* **197**, 1537–1550, doi: [10.1093/gji/ggt341](https://doi.org/10.1093/gji/ggt341).
- Massa, M., S. Lovati, E. D’Alema, G. Ferretti, and M. Bakavoli (2010). An experimental approach for estimating seismic amplification effects at the top of ridge, and the implication for ground-motion predictions: The case of Narni, central Italy, *Bull. Seismol. Soc. Am.* **100**, no. 6, 3020–3034, doi: [10.1785/0120090382](https://doi.org/10.1785/0120090382).
- Maufroy, E. (2010). Caractérisation et modélisation numérique de l’effet de site topographique 3D: Application à la Grande Montagne de Rustrel, Vaucluse, *Ph.D. Thesis*, University of Nice-Sophia Antipolis, France.
- Maufroy, E., V. M. Cruz-Atienza, and S. Gaffet (2012). A robust method for assessing 3-D topographic site effects: A case study at the LSBB Underground Laboratory, France, *Earthq. Spectra* **28**, no. 3, 1097–1115, doi: [10.1193/1.4000050](https://doi.org/10.1193/1.4000050).
- Moore, I. D., R. B. Grayson, and A. R. Ladson (1991). Digital terrain modelling: A review of hydrological, geomorphological, and biological applications, *Hydrolog. Process.* **5**, no. 1, 3–30, doi: [10.1002/hyp.3360050103](https://doi.org/10.1002/hyp.3360050103).
- Pischiutta, M., G. Cultrera, A. Caserta, L. Luzi, and A. Rovelli (2010). Topographic effects on the hill of Nocera Umbra, central Italy, *Geophys. J. Int.* **182**, no. 2, 977–987, doi: [10.1111/j.1365-246X.2010.04654.x](https://doi.org/10.1111/j.1365-246X.2010.04654.x).

- Poppeliers, C., and G. L. Pavlis (2002). The seismic response of a steep slope: High-resolution observations with a dense, three-component seismic array, *Bull. Seismol. Soc. Am.* **92**, 3102–3115.
- Rai, M., A. Rodriguez-Marek, and A. Yong (2012). Topographic effects in strong ground motion, in *Proc. of the 15th World Conference on Earthquake Engineering*, Lisboa, Portugal, 24–28 September 2012, Paper Number 3843.
- Rodriguez-Marek, A., F. Cotton, N. A. Abrahamson, S. Akkar, L. Al-Atik, B. Edwards, G. A. Montalva, and H. M. Dawood (2013). A model for single-station standard deviation using data from various tectonic regions, *Bull. Seismol. Soc. Am.* **103**, no. 6, 3149–3163, doi: [10.1785/B0120130030](https://doi.org/10.1785/B0120130030).
- Sánchez-Sesma, F. J. (1983). Diffraction of elastic waves by three-dimensional surface irregularities, *Bull. Seismol. Soc. Am.* **73**, no. 6A, 1621–1636.
- Sánchez-Sesma, F. J., and M. Campillo (1991). Diffraction of *P*, *SV*, and Rayleigh waves by topographic features: A boundary integral formulation, *Bull. Seismol. Soc. Am.* **81**, no. 6, 2234–2253.
- Spudich, P., M. Hellweg, and W. H. K. Lee (1996). Directional topographic site response at Tarzana observed in aftershocks of the 1994 Northridge, California, earthquake: Implications for mainshock motions, *Bull. Seismol. Soc. Am.* **86**, no. 1B, S193–S208.
- Strasser, F. O., N. A. Abrahamson, and J. J. Bommer (2009). Sigma: Issues, insights, and challenges, *Seismol. Res. Lett.* **80**, no. 1, 40–56, doi: [10.1785/gssrl.80.1.40](https://doi.org/10.1785/gssrl.80.1.40).
- Trifunac, M. D. (1972). Scattering of plane *SH* waves by a semi-cylindrical canyon, *Earthq. Eng. Struct. Dynam.* **1**, 267–281.
- Wong, H. L., M. D. Trifunac, and B. Westermo (1977). Effects of surface and subsurface irregularities on the amplitudes of monochromatic waves, *Bull. Seismol. Soc. Am.* **67**, 353–368.
- Zevenbergen, L. W., and C. R. Thorne (1987). Quantitative analysis of land surface topography, *Earth Surf. Process. Landf.* **12**, no. 1, 47–56, doi: [10.1002/esp.3290120107](https://doi.org/10.1002/esp.3290120107).

Univ. Grenoble Alpes  
 ISTerre, CNRS, IRD, IFSTTAR  
 F-38041 Grenoble, France  
 emeline.maufroy@ujf-grenoble.fr  
 fcotton@gfz-potsdam.de  
 (E.M., F.C.)

Instituto de Geofísica  
 Universidad Nacional Autónoma de México  
 04510 México D.F., Mexico  
 cruz@geofisica.unam.mx  
 (V.M.C.-A.)

GEOAZUR, UMR 7329  
 Université de Nice Sophia-Antipolis  
 CNRS, IRD, Observatoire de la Côte d'Azur  
 Sophia-Antipolis, F-06560 Valbonne, France  
 gaffet@geoazur.unice.fr  
 (S.G.)

Manuscript received 31 March 2014;  
 Published Online 2 December 2014